2013 IEEE International Conference on Robotics and Automation (ICRA)
Karlsruhe, Germany, May 6-10, 2013

Closed-Loop Commutation Control of an MRI-Powered Robot Actuator

Christos Bergeles, *Member, IEEE*, Panagiotis Vartholomeos, *Member, IEEE*, Lei Qin, and Pierre E. Dupont, *Fellow, IEEE*

***Abstract*— Actuators that are powered, imaged and controlled by Magnetic Resonance (MR) scanners offer the potential of inexpensively providing wireless control of MR-guided robots. Similar to traditional electric motors, the MR scanner acts as the stator and generates propulsive torques on an actuator rotor containing one or more ferrous particles. To generate maximum motor torque while avoiding instabilities and slippage, closed-loop control of the electromagnetic field gradients, i.e., commutation, is required. This paper proposes and demonstrates a method for commutation based on interleaving pulse sequences for rotor tracking and rotor propulsion. Fast rotor tracking is achieved by a new technique utilizing radio-frequency (RF) selective excitation of a properly located fiducial marker by the ferrous particle of the rotor. Optimal marker location is derived and demonstrated to provide accurate estimates of rotor angle. In addition, closed-loop commutation control is shown to increase motor torque and also to enable regulation of rotor angle.**

I. Introduction

Magnetically actuated devices are emerging tools for both diagnostic and interventional medical procedures. For example, endoscopes actuated by permanent magnets have been proposed for imaging the GI tract [1] and the stomach [2]. Custom electromagnetic control systems have been employed for intravascular [3] and intraocular [4] microrobot navigation. These magnetic actuation platforms require coupling to an imaging system, such as ultrasound [1], fluoroscopy [3], or surgical microscopy [4].

Since MRI delivers high amounts of non-ionizing electromagnetic energy, the scanners offer the potential for both electromagnetic energy transfer as well as imaging. Examples of this approach include an MR-powered swimming endoscope [5] and an intravascular swimming robot [6].

Centimeter-scale MRI-powered and imaged robots would be small enough to fit inside the bore to access hard-to-reach mid-torso locations or could even fit inside the body. While a variety of MR-compatible robots for surgical procedures ranging from brachytherapy to heart surgery have been developed [7]–[9], they all require actuators of high cost or high complexity and also necessitate either mechanical or electrical tethering to external control systems. An MRI-powered interventional device, however, may be fabricated inexpensively from plastic parts and ball bearings and can be actuated, imaged, and controlled directly by the MRI scanner.

This work was supported by the Wyss Institute for Biologically Inspired Engineering and by the National Institutes of Health under grant R01HL073647.

C. Bergeles, P. Vartholomeos, and P. E. Dupont are with the Department of Cardiovascular Engineering, Boston Children's Hospital, Harvard Medical School, 02115 Boston, Massachusetts {firstname.lastname@childrens.harvard.edu}.
Lei Qin is with Dana-Farber Cancer Research Institute, Harvard Medical School, 02115 Boston, Massachusetts {lqin2@partners.org}.

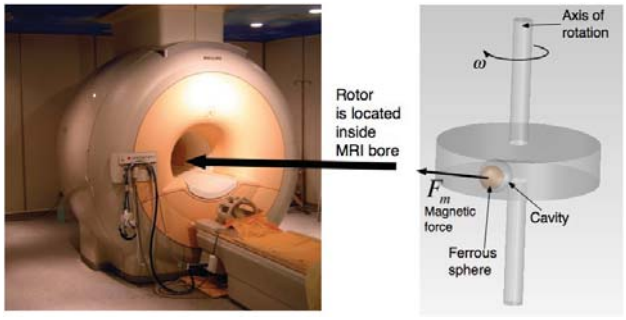

Fig. 1. MRI-powered actuator. Interleaved imaging and propulsion pulse sequences are used to track rotor angle and generate magnetic-gradient-based forces enabling control of both motor position and torque.

The contributions of this paper include a novel method for tracking ferromagnetic material in an MRI-invisible actuator and the first demonstration of commutation in an MRI-powered actuator. The paper is arranged as follows. The actuator technology is briefly described in Sec. II. In Sec. III, the tracking methodology is presented. Sec. IV describes the implementation of closed-loop gradient control. The experimental validation of the tracking algorithm, commutation control and rotor angle control is presented in Sec. V. Conclusions appear in Sec. VI.

II. MRI-Powered Actuator

The actuation technology, introduced in [10], can be explained by analogy to an electric motor. As Fig. 1 shows, the scanner and the chassis of the actuator comprise the stator. A rotor with an encapsulated ferrous sphere is the rotational part of the actuator. Rotating MRI gradients generate forces on the ferrous sphere, which causes rotor motion. Since the sphere is enclosed in a cavity, it is free to remain aligned with the scanner's $\vec{B}_0$ field during rotor rotation.

In brushless electric motors with encoders, maximum torque is produced via commutator control [see Fig. 2(a)]. The current in each electromagnet is controlled based on the Hall sensors' rotor angle estimation. The forces, F, generated on the rotor's permanent magnet by the electromagnets should be directed such that maximum torque is generated for all angular configurations of the rotor, i.e. the angle ψ in Fig. 2(a) should be $90°$. The commutator controller regulates ψ to this optimal value.

In our prior implementation of an MRI-powered actuator, commutation was performed open loop using sinusoidal gradients that were commanded to rotate at the desired angular

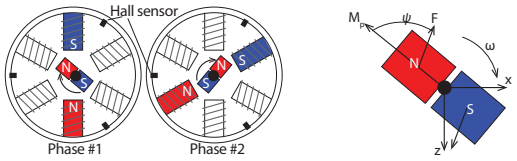

Fig. 2. Brushless DC motor. (a) Active electromagnets during rotor motion for two consecutive configurations. (b) Rotor forces F, and angle ψ.

rate of the motor [10]. While this approach enabled needle insertion using an outer position control loop, it possessed several limitations. For example, load perturbations would cause the rotor to slip such that the needle would stop moving for one or more revolutions of the magnetic gradients. In addition, since the angle ψ between the rotor and the magnetic force was not regulated, the actuator produced less torque. Finally, since position control was based on sensed needle position rather than rotor angle (at transmission input), displacement resolution was significantly reduced.

As in classic electric motors, commutator control of the rotor enables maximal torque generation as well as rotor angle control. To achieve these goals (1) the rotor angle needs to be tracked in real time, and (2) the direction of the applied gradients need to be controlled in closed loop. These topics are addressed in the next two sections.

III. Tracking Methodology

Tracking in MRI is categorized as active or passive. In active tracking, small receiver coils, which are tuned to the scanner's RF frequency, are hardwired to the MRI receiver channels to allow for electronic readout of their position [11]. Active tracking cannot be used in the context of a wireless and untethered robotic mechanism.

Passive tracking employs fiducial markers such as capsules containing liquids that produce high intensity MRI images. Consequently, they can be used outside tissue. For example, in [12], this approach was used to track a robotic arm.

Ferromagnetic particles can also be used as passive fiducials. Rather than produce a bright spot in an MRI image, however, they produce a signal void in the image. This arises since their magnetic field causes local inhomogeneities to the B_0 field of the MRI scanner, inducing significant signal dephasing which results in signal voids. If this void appears inside a region that would otherwise produce a signal, it appears as a dark blob, which can be detected and used for tool localization [13]. This approach cannot be employed outside tissue since it relies on detecting an image void.

Recently, [6], [14] demonstrated the use of ferromagnetic particles as positive markers located inside tissue [see Fig. 3(a)]. Instead of using RF pulses that correspond to the Larmor frequency of hydrogen in the presence of $\vec{B_0}$, the RF pulse frequency is selected to affect molecules that are in the $\vec{B_0} + \vec{B_p}$ field, where $\vec{B_p}$ is created by the ferrous particle. In this way, only water molecules that are in the vicinity of the ferromagnetic particle are excited (RF-selective excitation). By varying the RF frequency and bandwidth, different

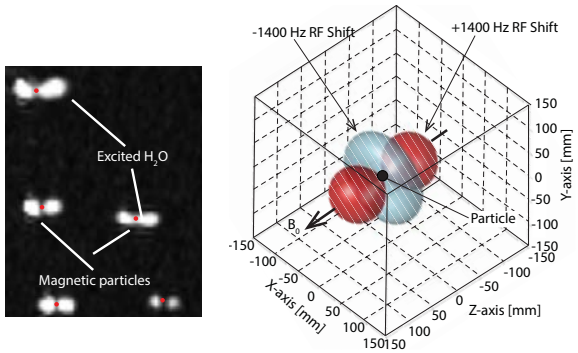

Fig. 3. (a) RF-selective excitation for magnetic particles (adapted from [14]), and (b) Simulation of the excited region for RF pulses shifted below and above the Larmor frequency.

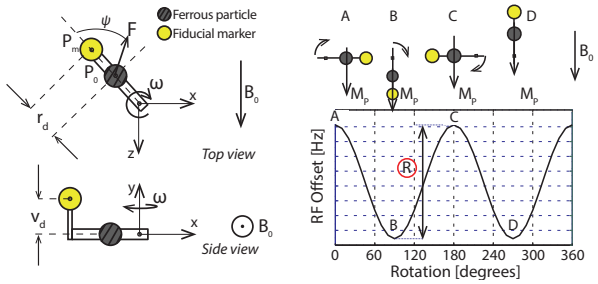

Fig. 4. Locating RF-selective fiducial marker on rotor. (a) Top view and side view of rotor. (b) Marker configuration example with $v_d = 0$ that requires configuration-dependent RF frequency to image marker. Rotor configurations of 0°, 90°, 180°, and 270° are indicated.

regions around the particle can be selected for excitation. Fig. 3(b) shows an example of the excited regions for RF frequencies above and below the Larmor frequency.

To track the rotor of the MRI-powered actuator, none of the approaches described above can be directly applied. Brightly imaging fiducial markers are rendered invisible when placed on the rotor due to the proximity of the ferrous sphere used for propulsion. Since the entire actuator is invisible to MRI, the void produced by the ferromagnetic sphere is also invisible. Furthermore, there are no nearby hydrogen atoms to excite using RF-selective excitation.

To track the rotor, we propose a new approach in which RF-selective excitation is used in combination with a positive image fiducial marker. In this approach, the fiducial marker is placed on the rotor in a specific configuration relative to the ferromagnetic sphere and an RF frequency and bandwidth are selected such that the fiducial marker appears brightly in the image regardless of rotor angle. Since the actuator is invisible, rotor angle tracking then reduces to tracking the fiducial marker in an otherwise void image region.

A. RF Frequency and Bandwidth Selection

Fig. 4(a) depicts the rotor showing both the ferrous sphere and the fiducial marker. The displacement of the marker relative to the sphere is given by the radial displacement, r_d and the vertical displacement, v_d. Note that a displacement in

the third relative coordinate direction is not considered here since its effect would be equivalent to the radial displacement as the rotor rotates with respect to candidate RF-excited regions [see Fig. 3(b)].

If the fiducial marker rotates in synchrony with the ferrous particle and can be continuously imaged using RF-selective excitation, localizing it will provide information on the rotor angle. We seek the values of the offset coordinates, r_d and v_d that enable angle-independent visualization of the marker. The ferromagnetic particle, modeled as a magnetic point-dipole, generates a field:

$$\vec{B}_p(\vec{M}_P, \vec{P}) = \frac{\mu_0}{4\pi\|\vec{P}\|^3}\left(\frac{3(\vec{M}_p \cdot \vec{P})\vec{P}}{\|\vec{P}\|^2} - \vec{M}_p\right) \quad (1)$$

where $\vec{M}_P$ [Am^2] is its magnetic moment, μ_0 [$\frac{\mathrm{Tm}}{\mathrm{A}}$] is the vacuum permeability, and $\vec{P}$ [m] is the vector connecting the point where the field is calculated and the point dipole. To image a fiducial marker positioned at $\vec{P_m}$, the central frequency of the RF pulse should account for $\vec{B}_P$, i.e.:

$$f = \frac{\gamma}{2\pi}\left[\vec{B}_p(\vec{M}_P, \vec{P}_m) + \vec{B}_0\right]\hat{z} = \frac{\gamma}{2\pi}\vec{B}_{\text{tot}}\hat{z} \quad (2)$$

where $\vec{B}_0$ is the homogeneous MRI field, γ [$\frac{\mathrm{rad}\times\mathrm{Hz}}{\mathrm{T}}$] is the gyromagnetic ratio of hydrogen and $\hat{z}$ is the unit vector along the MRI bore axis.

As the rotor rotates, the ferrous particle rotates so as to maintain its magnetic alignment with B_0 while its relative location with respect to the fiducial marker changes. Thus, the fiducial marker is exposed to a varying magnetic field $\vec{B}_{\text{tot}}$ and would need to be imaged by RF pulses of varying central frequency in order to remain excited.

Fig. 4(b) illustrates this scenario for the case of $\mathrm{v}_d = 0$. It can be seen that the RF offset frequency varies periodically with rotor angle. This creates an implicit tracking problem wherein knowledge of the appropriate RF frequency is required for tracking, but the marker's location is a prerequisite. While an implicit tracking formulation is possible, it is more computationally intensive than an explicit one. Thus, it is observed that the optimal fiducial marker position should result in an explicit formulation, i.e., such that a single RF offset frequency applies for all rotor angles.

To achieve maximum signal response for a spherical fiducial marker of radius r [m], its full volume should be excited by the range of frequencies contained within the RF pulse. Thus, the bandwidth of the RF pulse should be selected as:

$$\vec{P}_{\text{far}} = \vec{P}_m + \frac{\vec{P}_m - \vec{P}_0}{\|\vec{P}_m - \vec{P}_0\|}r \quad (3)$$

$$\vec{P}_{\text{near}} = \vec{P}_m - \frac{\vec{P}_m - \vec{P}_0}{\|\vec{P}_m - \vec{P}_0\|}r \quad (4)$$

$$\text{BW} \geq \frac{\gamma}{2\pi}\left|\left[\vec{B}_p(\vec{M}_P, \vec{P}_{\text{far}}) - \vec{B}_p(\vec{M}_P, \vec{P}_{\text{near}})\right]\hat{z}\right| \quad (5)$$

where $\vec{P}_0$ is the location of the point dipole [see Fig. 4(a)].

Since the actuator will be placed in proximity to tissue, the RF pulse should avoid tissue excitation by not containing the Larmor frequency corresponding to $\vec{B}_0$:

$$f - \frac{\text{BW}}{2} > \frac{\gamma}{2\pi}\vec{B}_0\hat{z}, \text{ or} \quad (6)$$

$$f + \frac{\text{BW}}{2} < \frac{\gamma}{2\pi}\vec{B}_0\hat{z} \quad (7)$$

Equations (2)-(7) can be used to optimize for variables r_d and v_d while additionally selecting the central frequency f and bandwidth BW. Sec. V provides results of this analysis.

IV. Closed-Loop Gradient Control

With the RF frequency and bandwidth selected, the fiducial marker can be imaged in the presence of the ferromagnetic particle. Commercial MR imaging sequences, however, do not operate in real time. To achieve real-time tracking, we use single-dimensional gradient echo pulse sequences, as in [6], [14]. These sequences have short gradient durations and do not generate unwanted rotor motion. They are termed "single-dimensional" because they do not perform phase encoding and provide an aggregate signal in one dimension. Since the gradient $\nabla\vec{B}_{\text{tot}}$ is affecting the fiducial marker, no slice-select gradient is required.

Fig. 5(a) shows the tracking pulse sequence and Fig. 5(b) the system architecture used to perform real-time gradient control. Tracking is performed only along x and z, since the ferrous particle is rotating in the xz-plane, with: TE $=$ 3.5 ms, TR $=$ 13 ms, FOV $=$ 300 mm, $\alpha = 80°$, and matrix $=$ 256 pixels. The selected FOV and matrix provide a 1.17 mm spatial resolution.

A high controller rate is crucial for commutation control and this tracking pulse sequence is executed in $t_{\text{track}} = 26$ ms. Subsequently, with a latency of 2 ms, the single-dimensional projections are transferred to the image processing workstation, where localization via peak detection is performed [see Fig. 5(a) for flowchart]. The estimated rotor angle is used to calculate the direction of actuating gradients so as to achieve a relative angle of $\psi = 90°$ [Recall Fig. 2(b)].

Due to the interleaving of tracking and actuation, as implemented in Fig. 5(a), there is no localization update during the period of actuation, t_{act}. Since the rotor is typically moving, the difference between ψ and its desired value can accumulate over the actuation period. Thus, there is tradeoff in this implementation between the total time spent on actuation during a control cycle and the effectiveness of actuation as measured by angle ψ as well as motor torque generated. This tradeoff is explored in the following section.

V. Experiments

To evaluate the tracking and commutation control methods described above, a series of analysis and experiments were performed using the prototype needle driving robot shown in Fig. 6. The system consists of a rotor driving a gear train attached to a rack. While for previous experiments, a rack-mounted needle was used to perform tissue insertion experiments [15], for the purpose of the experiments described below, the needle was removed and, for some tests, a calibrated spring was attached to generate a linear load.

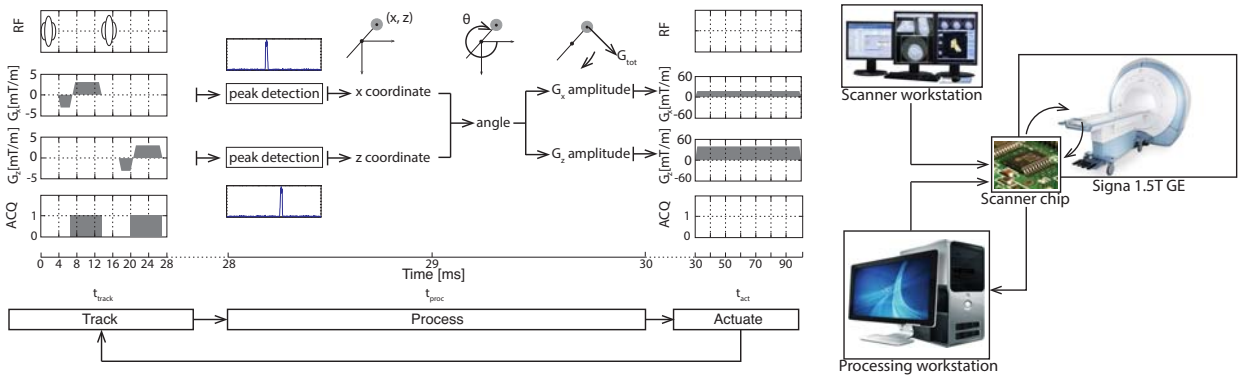

(a) (b)

Fig. 5. (a) Schematic of the tracking sequence and algorithm flowchart, and (b) control system and information workflow.

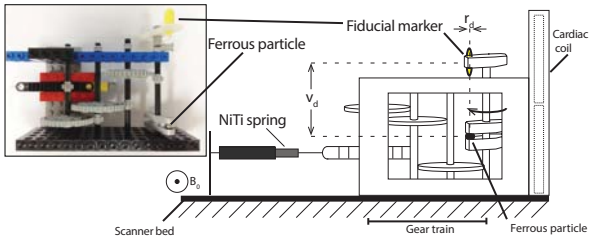

Fig. 6. Illustration of the experimental setup.

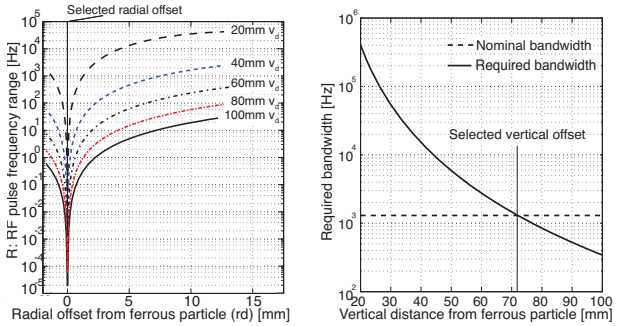

(a) (b)

Fig. 7. Selection of marker location. (a) Dependency of the RF pulse on r_d for different values of v_d. (b) Dependency of the RF bandwidth on v_d. Dashed line represents the bandwidth corresponding to standard 3.2 ms RF.

The prototype is constructed from LEGO blocks. It is MRI-invisible, and its parameters are given in Table I. Real time communication was achieved using a socket-based protocol developed for the Signa 1.5 T GE scanner, RTHawk [16].

A. RF Central Frequency and Bandwidth Selection

An MR-SPOT (Beekley Medical, CT) marker's location was optimized for the ferrous particle contained within the actuator, as described in Sec. III. Fig. 7(a) shows the range of frequencies required for various displacements r_d. This simulation shows that to use an RF pulse with constant central frequency for varying rotor angles, there should be no radial displacement of the fiducial marker with respect to the ferrous particle, i.e. $r_d = 0\,\mathrm{mm}$.

The required RF-pulse bandwidth with respect to the vertical distance v_d is shown in Fig. 7(b). The dashed line corresponds to the bandwidth of a 3.2 ms RF pulse (1.3 kHz), which is a nominally used duration. As a result, it was chosen that $\mathrm{v}_d \geq 72\,\mathrm{mm}$, and the full marker volume could be excited using the nominal bandwidth (see Fig. 8).

Parameter	Value
Radius of ferrous sphere	3 mm
Saturation magnetization of ferrous sphere	1.36×10^6 A/m
Lever radius	16.8 mm
Transmission ratio	25×10^3
Fiducial marker radius	3.5 mm
Fiducial marker height	16 mm
r_d, v_d	~ 0.5 mm, ~ 74 mm
$\|\vec{B}_0\|$	1.5 T

TABLE I

PROTOTYPE ACTUATOR PARAMETERS

These selections of r_d and v_d define $\vec{P}_m(r_d, \mathrm{v}_d)$ and (1)-(2) can now be used to solve for $f = -1200\,\mathrm{Hz}$. Given the choice of BW $= 1.3\,\mathrm{kHz}$ in the paragraph above, it can be verified that these values satisfy (7) ensuring that no signal emission from tissue will arise during fiducial tracking. The resulting volume of excitation around the ferrous sphere is depicted in Fig. 8. It is observed that the fiducial marker (shown as pill shaped) is entirely within the excited region. Moreover, the conducted analysis guarantees that its excitation is independent of rotor angle.

B. Tracking

Imaging was performed using a cardiac surface coil (see Fig. 6). Tracking is initialized using a calibration procedure to identify the axis of rotation. This is performed by locking the rotor at four orthogonal configurations corresponding to 0°, 90°, 180°, and 270°. Using the positions estimated at these configurations, the center of rotation is calculated. Using the calculated coordinates, tracking accuracy was evaluated for angles between 0° and 360° with 22.5° steps.

Fig. 9 and Table II shows that all angles can be estimated with a mean error of $2.6° \pm 1.3°$. No filtering was performed, but outliers could have been rejected based on their estimated distance from the circle center. Theoretically, for the rotation radius of $r = 16.8\,\mathrm{mm}$ (see Table I) and the calculated

TABLE II

ANGLE-ESTIMATION PERFORMANCE (MEAN AND STANDARD DEVIATION)

	Angles [°] (no water)															
	0	22.5	45	67.5	90	112.5	135	157.5	180	202.5	225	247.5	270	292.5	315	337.5
μ	0.2	25.7	44.9	67.2	92.3	114.5	138.6	161.7	183.0	205.9	227.7	248.9	274.0	297.6	319.9	342.0
σ	0.05	1.1	1.1	0.7	2.3	0.4	2.8	2.2	1.8	1.7	2.1	2.8	2.1	2.1	1.6	0.7
	Angles [°] (water)															
μ	−6.4	13.7	38.9	65.7	93.3	119.3	149.8	166.9	187.1	202.6	229.2	248.1	268.3	290.5	309.6	333.0
σ	0.9	1.6	1.1	2.3	1.0	2.2	9.9	3.2	4.6	11.5	1.6	1.3	1.5	1.2	1.8	1.5

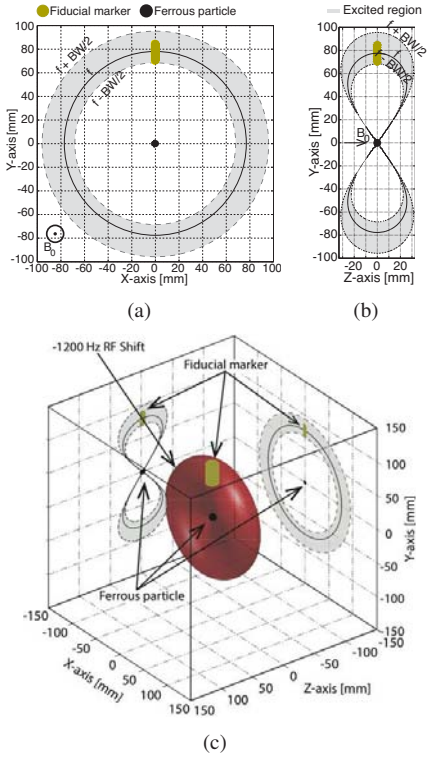

Fig. 8. Region of RF-selected excitation. (a) XY plane, (b) ZY plane, (c) 3D view with projections. Solid lines indicate surface excited at central RF frequency; dashed lines indicate volume excited over bandwidth.

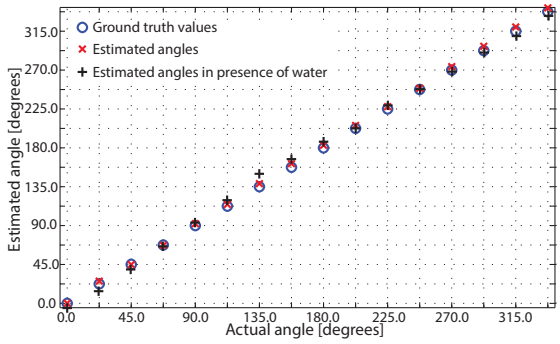

Fig. 9. Localization results for various angles. Blue ○: nominal angles, red ×: calculated angles, black +: calculated angles in the presence of water.

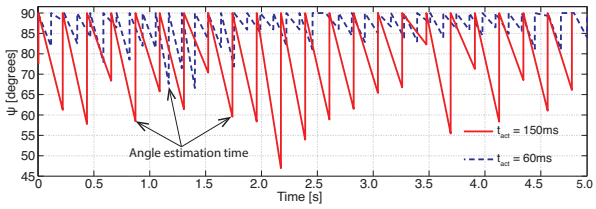

Fig. 10. Commutator control achieves operation near a slip angle of 90°, depending on the selection of t_{act}.

spatial resolution, the expected angular resolution is $\sim 5°$. The estimations are at the limits of this resolution.

The performance of the algorithm was also evaluated with respect to tissue presence. To simulate tissue, a water container was placed on the rack side of the actuator. As discussed in Sec. III, the employed RF-selective pulses should not excite water molecules, since the contribution of $\vec{B}_p$ at their location is minimal. As shown in Fig. 9 and Table II, high angular resolution is indeed possible with a mean error of $5.1° \pm 1.7°$, which is at the limits of the resolution.

Given the gear ratio of the robot, a full rotor rotation equates to $0.25\,\text{mm}$ rack translation. With the achieved angular resolution, fine tip motion on the order of $\pm 0.004\,\text{mm}$ can be detected. This is a significant improvement over our previously reported tip tracking results of ± 1.37 mm [15].

C. Closed-Loop Gradient Control

To evaluate the ability of the controller to maintain the desired angle between rotor and gradient direction at $\psi = 90°$ and the effect that this has on torque production, the rack of the actuator was connected to a calibrated MR-compatible NiTi spring ($k = 35\frac{\text{N}}{\text{m}}$) as shown in Fig. 6. A set of experiments were performed in which the actuation time, t_{act}, was varied in the control loop shown in Fig. 5(a). Spring extension, computed using rotor tracking, was used to measure force produced by the rack.

Fig. 10 illustrates the tradeoff between the duration of the actuation sequence and the error in actuation direction that accumulates over an actuation cycle. At the start of each actuation cycle, the angle ψ is set to 90°. At this optimal angle, gradient direction leads rotor angle by 90°. At the next tracking time, ψ can be seen to have decreased indicating that the rotor has partially caught up with the gradients leading to a loss of torque produced. The shorter actuation time, $t_{\text{act}} = 60\text{ms}$, leads to significantly smaller variations in ψ.

To evaluate the effect on force production, Fig. 11 depicts measured spring force for actuation times of $t_{\text{act}} = \{60, 100, 150, 200\}$ ms. In open loop, the spring extension was recored by a camera and measured via image processing. The force produced without commutator control (open loop) at $1\,\text{Hz}$ is also shown with points of rotor slip marked. No rotor slip was observed under closed-loop control. The percentage change in output force compared with open-loop

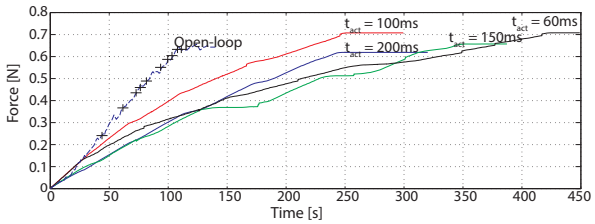

Fig. 11. Force experiments. Dashed blue line: open-loop gradient control. Solid lines: closed-loop gradient control. Black +: rotor slipped cycles.

t_{act} [ms]	60	100	150	200
Closed-loop force [mN]	704	705	659	618
% increase	9.66	9.81	2.65	−3.73

TABLE III

EXPERIMENTAL FORCES [N] AND TORQUE INCREASES [%]

control is given in Table III. It can be seen that there is an increase in maximum output torque on the order of 10%, which occurs for $t_{\text{act}} = 100\,\text{ms}$. Additionally, it should be noted that production of maximum torque under open-loop control required an elastic load [10] whereas with commutation control, the maximum torque can delivered against arbitrary loads.

D. Closed-Loop Rotor Angle Control

To demonstrate the capability to implement an outer rotor position control loop around an inner commutation control loop, rotor angle regulation experiments were performed. For these trials, the actuator was decoupled from the spring and and outer PID loop was synthesized. In this approach, the inner commutation loop computes gradient direction while the outer position loop computes gradient amplitude based on rotor angle error. The parameters P, I, D where tuned manually ($P = 0.01\,\text{rad}^{-1}$, $D = 0, I = 5 \times 10^{-5}\,\text{rad}^{-1}$). Fig. 12 demonstrates the step response for four commanded angles. Steady-state position errors can be seen to lie within the $\pm 5^\circ$ resolution of the tracking algorithm.

VI. CONCLUSIONS AND DISCUSSION

Actuators that are wirelessly powered, imaged and controlled using MR scanners constitute a new actuation technology that enables the exploration of many new design ideas in medical robotics. Since this approach differs fundamentally from traditional MR programming, its development poses interesting and challenging engineering problems.

This paper has addressed several fundamental challenges. First, it has proposed a new approach to tracking of ferrous material by generating RF-selective signatures in properly located fiducial markers. Second, it has employed this tracking method for closed-loop commutation control of an MRI-powered actuator. Demonstrated benefits include: (a) slippage of the actuator is avoided, (b) angle control on the rotor is possible, and (c) the generated torque increases.

Future work will involve improving transmission efficiency through the use of alternate materials, and investigation of the simultaneous tracking and actuation of multiple motors.

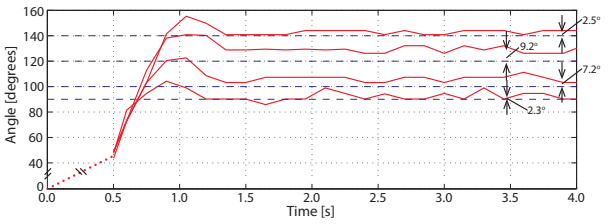

Fig. 12. Example of rotor angle control using a simple PID controller for target angles = $\{90^\circ, 100^\circ, 120^\circ, 140^\circ\}$.

ACKNOWLEDGEMENTS

The assistance of Drs. Ehud Schmidt and Ferenc Jolesz (Brigham & Women's Hospital) is gratefully acknowledged.

REFERENCES

[1] S. Tognarelli, V. Castelli, G. Ciuti, C. Di Natali, E. Sinibaldi, P. Dario, and A. Menciassi, "Magnetic propulsion and ultrasound tracking of endovascular devices," *J. Robotic Surgery*, 2012, online.

[2] S. Yim and M. Sitti, "Design and rolling locomotion of a magnetically actuated soft capsule endoscope," *IEEE Trans. Robotics*, vol. 28, no. 1, pp. 183–194, 2012.

[3] C. Yu, J. Kim, H. Choi, J. Choi, S. Jeong, K. Cha, J. Park, and S. Park, "Novel electromagnetic actuation system for three-dimensional locomoation and drilling of intravascular microrobot," *Sensor and Actuators A: Physical*, vol. 161, pp. 297–304, 2012.

[4] C. Bergeles, M. P. Kummer, B. E. Kratochvil, C. Framme, and B. J. Nelson, "Steerable intravitreal inserts for drug delivery: *in vitro* and *ex vivo* mobility experiments," *Int. Conf. Medical Image Computing and Computer Assisted Intervention*, pp. 33–40, 2011.

[5] G. Kósa, P. Jakab, G. Székely, and N. Hata, "MRI driven magnetic microswimmers," *J. Biomed. Microdev.*, vol. 14, pp. 165–178, 2012.

[6] A. Chanu, O. Felfoul, G. Beaudoin, and S. Martel, "Adapting the clinical MRI software environment for real-time navigation of an endovascular untethered ferromagnetic bead for future endovascular interventions," *Mag. Res. Med.*, vol. 59, pp. 1287–1297, 2008.

[7] D. Y. Song, E. C. Burdette, J. Fienne, E. Armour, G. Kronreif, A. Deguet, Z. Zhang, I. Iordachita, G. Ficthinger, and P. Kazanzides, "Robotic needle guide for prostate brachytherapy: clinical testing of feasibility and performance," *Brachytherapy*, vol. 10, pp. 57–63, 2011.

[8] H. Su, D. C. Cardona, W. Shang, A. Camilo, G. A. Cole, D. C. Rucker, R. J. Webster III, and G. S. Fischer, "A MRI-guided concentric tube continuum robot with piezoelectric actuation: a feasibility study," *IEEE Int. Conf. Robotics and Automation*, pp. 1939–1945, 2012.

[9] N. V. Navkar, Z. Deng, D. J. Shah, K. E. Bekris, and T. N. V., "Visual and force-feedback guidance for robot-assisted interventions in the beating heart with real-time MRI," *IEEE Int. Conf. Robotics and Automation*, pp. 689–694, 2012.

[10] P. Vartholomeos, L. Qin, and P. E. Dupont, "MRI-powered actuators for robotic interventions," *IEEE/RSJ Int. Conf. Intelligent Robots and Systems*, pp. 4508–4515, 2011.

[11] L. Qin, E. J. Schmidt, Z. T. H. Tse, J. M. Santos, W. S. Hoge, C. Tempany-Afdhal, K. Butts-Pauly, and C. L. Dumoulin, "Prospective motion correction using tracking coils," *Mag. Res. Med.*, 2012.

[12] G. Thörmer, N. Garnov, M. Moche, J. Haase, T. Kahn, and H. Busse, "Simultaneous 3D localization of multiple MR-visible markers in fully reconstructed MR images: proof-of-concept for subsecond position tracking," *Magnetic Resonance Imaging*, vol. 30, pp. 371–381, 2012.

[13] H. Busse, R. Trampel, W. Gruünder, M. Moche, and T. Kahn, "Method for automatic localization of MR-visible markers using morphological image processing and conventional pulse sequences: feasibility for image-guided procedures," *J. Magnetic Resonance Imaging*, vol. 28, pp. 1087–1096, 2007.

[14] C. H. Cunningham, T. Arai, P. C. Yang, M. V. McConnell, J. M. Pauly, and S. M. Conolly, "Positive contrast magnetic resonance imaging of cells labeled with magnetic nanoparticles," *Magnetic Resonance in Medicine*, vol. 53, pp. 999–1005, 2005.

[15] C. Bergeles, L. Qin, P. Vartholomeos, and P. E. Dupont, "Tracking and position control of an MRI-powered needle-insertion robot," *IEEE Int. Conf. Engineering in Medicine and Biology*, pp. 928–931, 2012.

[16] (2012) HeartVista, Inc. [Online]. Available: www.heartvista.com